JTTEE5 14:215-223
DOI: 10.1361/10599630523773
1059-9630/$19.00 © ASM International

Peer Reviewed

Microstructure and Failure Mechanism in As-Deposited, Vacuum Plasma-Sprayed Ti-6Al-4V Alloy

H.R. Salimijazi, T.W. Coyle, J. Mostaghimi, and L. Leblanc

(Submitted September 3, 2003; in revised form March 3, 2004)

The microstructure, phase composition, and chemical composition of vacuum plasma-sprayed Ti-6Al-4V alloys were examined in detail using a variety of techniques, including x-ray diffraction, x-ray photoelectron spectroscopy, and transmission electron microscopy. The observed chemistry and structure were related to the conditions under which the deposit was formed and the phase equilibria in the Ti alloy system. The porosity of the deposit was in the range of 3 to 5%. A slight decrease in the Al content and a slight increase in the amount of oxygen and hydrogen was found relative to the starting powder. Within individual splats, a columnar solidification structure can be seen. However, the as-deposited material is ≥90% α′ martensite that is present in the form of fine lathes on the order of 500 nm in width surrounded by residual β-phase. This herringbone structure obscures to some extent the preexisting columnar structure of the as-solidified β-phase. The material fails at low elongations (~1%) when tested in tension, with a macroscopic stress-strain curve, which appears to be quite brittle. Examination of the fracture surface, however, reveals a ductile failure mode within individual splats, which is consistent with the structure described above. Sections perpendicular to the fracture surface show that failure occurs at the weak splat boundaries through the development and growth of voids between splats.

Keywords characterization, failure mechanism, mechanical properties, microstructure, Ti-6Al-4V, vacuum plasma spraying

1. Introduction

The vacuum plasma spray (VPS) process has been used for over 20 years to deposit a thin layer of protective coating on a variety of substrates to improve surface properties such as wear resistance, corrosion resistance, and thermal stability. Recently, VPS forming (VPSF) was identified as a process that is capable of manufacturing near-net-shaped components for applications in aerospace, the chemical process industry, and defense. Ti-6Al-4V alloys are widely used in these and other industrial sectors due to good stability at high temperature, high specific strength, especially at high operating temperatures, and high corrosion resistance in many corrosive media (Ref 1-4). In this study, the microstructure and mechanical behavior of the VPSF Ti-6Al-4V alloy is examined.

Because the quality requirements for VPSF materials that are intended for structural applications are different from the requirements for coatings, simple microstructural characteristics such as porosity, oxide content, powder and splat morphology, and solidification structure do not fully address the microstructure requirements, which must be met to assure optimal properties. As with any structural materials, metallurgical considerations such as grain size, phase composition, and phase distribution must be considered for the VPSF structures. On the other hand, microstructures of the VPSF materials are different from cast and forged structures due to the high cooling rate during solidification, the impact of molten powders on the substrate or prior deposition, the large thermal gradient during deposition, a lamellae type microstructure, and the existence of unmelted and partially melted powders in the microstructure. Moreover, due to the absence of convectional heat transfer from the substrate or prior deposition and more interaction between the plasma jet and the substrate, the VPSF deposit is maintained at a high temperature (up to 1000 °C) during the process. This results in microstructural evolution during the process, including recrystallization, polygonization, and stress relief, thereby enhancing intersplat bonding (Ref 5).

To study solidification during VPSF, researchers have examined a number of nickel-based alloys (Ref 1-5). Their results show that the rapid solidification of the molten droplets occurs during deposition in a low-pressure environment, with the deposits achieving nearly theoretical density. They reported that even in the case of heating the substrate up to 900 °C during the deposition, the cooling rates were likely to be equivalent to those of rapid solidification processes (i.e., 10^6 to 10^7 K/s). Several studies on particle temperature, velocity, and solidification during VPS have been reported. Zhao et al. (Ref 1, 2) have developed a numerical model to calculate the distribution of plasma gas temperature, enthalpy, and velocity under a range of plasma currents, gas flow rates, and chamber pressures for Ti particles in VPS. Sampath and Herman (Ref 5) have reviewed solidification parameters, morphological stabilities, and cooling rates for Ni, Al, and Mo using various techniques such as dendrite arm spacing and splat thickness correlation. They reported cooling rates

---

H.R. Salimijazi, T.W. Coyle, and **J. Mostaghimi,** Centre for Advanced Coatings Technologies, University of Toronto, Toronto, Canada; and **L. Leblanc,** formerly with PyroGenesis Inc., Montreal, Canada. Contact e-mail: tom.coyle@utoronto.ca.

Table 1 Chemical composition of Ti-6Al-4V powders

	Composition, wt.%				Composition, ppm		
Element	25-45 µm	45-63 µm	63-75 µm	Element	25-45 µm	45-63 µm	63-75 µm
Al	5.94	6.02	5.87	C	240	<100	210
V	3.95	3.98	3.99	O	980	820	750
Fe	0.084	0.086	0.082	H	27	10	15
Ni	0.016	0.017	0.017	N	80	70	80
Cr	0.019	0.019	0.018	…	…	…	…
Ti	Balance	Balance	Balance	…	…	…	…

on the order of 10^7 to 10^8 K/s for splat solidification during VPS. Literature reports indicate that the splat cooling rates depend not only upon substrate or prior deposit temperature, but also on substrate thermal conductivity. Deposition on a low-thermal-conductivity substrate or prior coating as well as high substrate temperatures show an order of magnitude lower cooling rates compared with those with a lower substrate temperature and higher thermal conductivity (Ref 5). This article examines microstructural development in the Ti-6Al-4V alloy during VPS and correlates the microstructural features with the tensile failure mechanisms. It is anticipated that such analyses will lead to better control of the deposit microstructure and, consequently, of the material properties.

Table 2 Vacuum plasma spray parameters

Gun	F4VB, Plasma–Tecknik
Current, A	800
Total gas flow rate, (Ar, H_2, He), slpm	60
Secondary gas proportion, (H_2, He), %	30
Powder carrier gas (Ar), slpm	2
Feed rate, g/min	30
Chamber pressure, mbar	140
Spray distance, mm	300
Substrate temperature, °C	700

2. Experimental Procedure

The specimens were made by the deposition of various powder sizes of standard feedstock Ti-6Al-4V powders (Table 1) produced by PyroGenesis Inc. (Montreal, Canada) using a vacuum plasma spraying process. An F4VB gun from Plasma–Tecknik (Luzern, Switzerland) was used in a low-pressure controlled atmosphere chamber. To form near-net-shaped structures, a copper mandrel mold was used. The temperatures of the mandrel as well as the prior deposit were maintained at approximately 750 °C during the spraying. The typical spray parameters are summarized in Table 2.

The oxygen content of the powders was determined using a LECO (St. Joseph, MI) carrier hot gas extraction analyzer. The chemical compositions of the powders and the as-sprayed structures were obtained from inductively coupled plasma mass spectroscopy. Two techniques of porosity measurement were used, mercury intrusion porosimetry (MIP) and image analysis (IA) on cross-section images by optical and scanning electron microscopy (SEM). A Measurescope-11 microscope (Nikon, Tokyo, Japan) was used for optical microscopy. SEM and energy-dispersive x-ray spectroscopy (EDS) was conducted on an Hitachi (Tokyo, Japan) S-4500 microscope.

Two types of specimens were prepared for transmission electron microscopy (TEM): cross sections; and sections parallel to the surface of the deposit. They were produced by mechanically grinding and polishing to a 20 µm thickness followed by jet polishing to form electron transparent regions. The TEM observation was performed using a transmission electron microscope (H-800; Hitachi) that was operated at 200 kV. X-ray diffractometry was performed on a Siemens D5000 diffractometer system (Siemens, Madison, WI), using a high-power Cu Kα source operating at 50 kV/35 mA over an angular range of $30° < 2\theta < 90°$. The diffracted beam was monochromatized by a Kevex solid-state detector (Kevex, Madison, WI). Surface hardness measurements were conducted using a Vickers indenter in a Zwick hardness tester (Zwick, Ulm, Germany) under a load of 2000 gram force (gf).

3. Results and Discussion

3.1. Initial Powders

Powder characteristics have been known to play a critical role in the quality of the as-sprayed structure. Factors such as chemical composition, impurities, size distribution, and morphology will directly affect the properties of the structures as well as the spraying process. For the VPSF of Ti-6Al-4V, a powder with low levels of contamination, a high degree of chemical uniformity, and a spherical morphology is desired. In this study, various particle sizes of titanium alloy powders were used to form freestanding structures. The free-flowing plasma-atomized powder of the Ti-6Al-4V alloy used in the VPSF process is shown in Fig. 1.

The chemical compositions of the powders are given in Table 1. The level of oxygen and hydrogen in the initial powders decreased with increasing the powder size. It can be assumed that the oxygen and hydrogen are stored in a thin layer on the surface of the powder. Therefore, oxygen and hydrogen in the powders are proportional to the reciprocal value of the average powder size (Ref 6). The x-ray diffraction (XRD) pattern of the powders is plotted in Fig. 2. Compared with the reference patterns of both α-hexagonal and β-body-centered cubic (bcc) Ti, the main phase is found to be αTi in the initial powder. It is worth noting that all reflections are quite broad. This means that in the powders, the αTi phase appears with a strained lattice, suggesting that a metastable α'-phase (martensite) had formed due to the rapid cooling.

3.2. As-Sprayed Structure

3.2.1 Physical and Mechanical Properties. The plasma-sprayed deposits consist of billions of individual splats that are connected together by mechanical and chemical bonding. The interlamellar boundaries are also associated with significant porosity, which depends on the thermal spray process parameters.

Krepski (Ref 4) has claimed that perhaps only 20 to 30% of the intersplat boundaries can be viewed as microwelds (depending on the process). Therefore, the physical and mechanical properties of such deposits mainly depend on the cohesive strength between the splats, and the size and morphology of the porosity, the cracks, and defects, and less on the microstructure within the splats themselves (Ref 5).

Chemical compositions of the as-sprayed structures using various sizes of initial powders are shown in Table 3. Decomposition of the initial powders during the spraying process causes a decrease in the aluminum content in the as-sprayed samples. Because hydrogen is used as a part of the plasma gas (Table 2) during the spraying, and because of the leakage of oxygen into the system, a pick up of hydrogen and oxygen can be observed. Furthermore, with increasing powder size, an increase in oxygen content of the as-sprayed structure can be noticed. A possible explanation is that, before the hot-sprayed particle is cooled down or oversprayed by the next droplet, it reacts with oxygen in the surrounding atmosphere. Due to the higher heat content, the larger droplets have lower cooling rates, and therefore more oxygen can react with the coarser-sprayed particles (Ref 6).

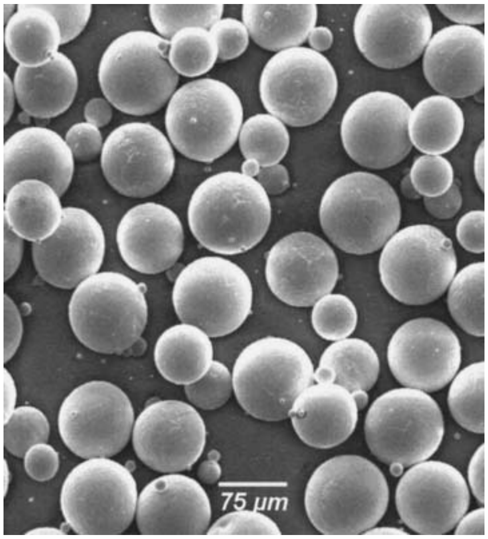

Fig. 1 Micrograph (SEM) of Ti-6Al-4V powder

As Fig. 3 illustrates, an EDS line scan through about 70 μm of the cross section of the VPSF structure, which consists of about eight individual splats, verifies the very uniform distribution of alloy elements such as Al and V as well as Ti, even in the lamellae boundary. There are some variations in the Al content in the pores located at the lamellae boundary and within the splats.

The measurement of porosity level by IA shows that the as-sprayed structures have an average porosity of 3%. Moreover, IA shows that the porosity slightly increases with increasing initial powder particle size. The MIP results show that the amount of open porosity varies slightly with powder particle size. The porosity is 0.7%, 1.8%, and 0.08%, and the average pore size is about 0.11 μm, 0.1 μm, and almost zero, respectively, for fine, medium, and coarse powders. It is worth noting that the value of porosity for the coarse powder structure is due to the roughness on the surface of sample; there is no mercury penetration and therefore no open porosity in the sample.

Hardness measurements on the cross sections indicate the intersplat strength within the structure, and are reflective of the phase present as well as the porosity distribution and content. The hardness results are 271, 285, and 301 HV, respectively, for fine, medium, and coarse powders. The higher value of hardness in the coarse powder structure is probably due to a lower level of porosity and therefore to the higher intersplat strength in the microstructure.

Tensile strength tests confirm that the tensile strength and yield strength of materials deposited using the two larger particle size distributions (i.e., the strength of large-particle materials) were significantly higher than the material deposited using the powder with the smallest particle size (700 MPa). Results show

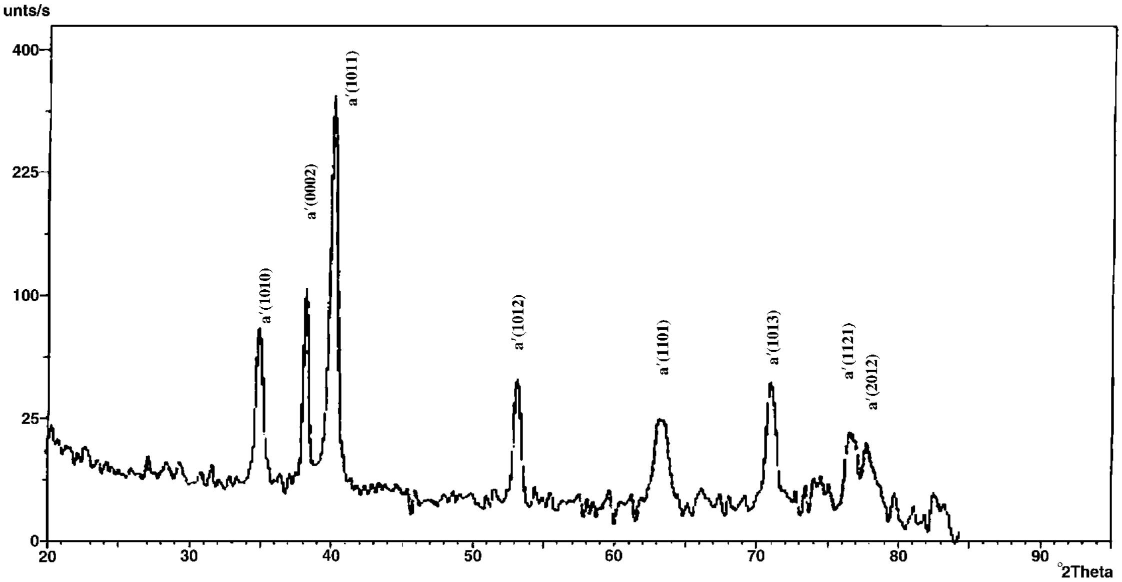

Fig. 2 XRD pattern of Ti-6Al-4V powders

that although the value of the tensile strength for the samples deposited using the two largest particle sizes were close to those of conventionally processed Ti-6Al-4V specimens, the ductility was as low as 1%, compared with 10 to 15% in the conventional materials.

3.2.2 Microstructure Development. Under low-to-medium cooling rates, three solidification front morphologies are formed: planar; cellular; and dendritic. The stable morphology is determined by the temperature gradient or solute gradient in the liquid. In the case of high cooling rates such as those in the rapid solidification process range, the stable growth morphology is a planar growth front (Ref 5).

Microstructural development in VPSF is mainly dependant on the solidification of the individual splats, as well as their position in the deposit. Earlier models for the solidification of individual splats showed a brick wall grain structure for the core region of the splat, while more recent models (Fig. 4) confirm columnar grain structures (Ref 5).

Figure 5 shows typical SEM micrographs of an etched VPSF Ti-6Al-4V alloy. The micrographs show clearly the columnar grain structures within the center core of the splat, which are oriented in the direction of heat transfer into the prior splats. The higher-magnification image reveals the presence of two phases. The gray (more deeply etched) regions are the α' lathes, which are separated by small white regions of remnant β-phase. The scale of the structure is quite fine, with the width of the α' lathes on the order of 0.5 µm. The micrographs also indicate fusion or microweld areas across the individual splats. Some internal porosity within several splats can be observed. Optical micrographs of etched (Fig. 6a) surfaces show the presence of some nonmelted and partially melted particles in the as-sprayed structure, especially for the coarse powder size. The lamellae boundaries are not distinct in the unetched micrograph (Fig. 6b); however, a few isolated larger pores, 10 to 15 µm in diameter, can be seen.

3.2.3 Transmission Electron Microscopy Observation. Due to the phase transformation (β to martensite) after the solidification of the alloy, the internal columnar substructure formed during solidification cannot be observed clearly by TEM. The most frequently observed structures in the TEM examinations of the lateral and cross sections were irregularly shaped, fine, equiaxed grains and a herringbone platelet structure (Fig. 7). Moreover, SEM micrographs from the TEM sample show a lath or platelet structure within the columnar substructure that is indicative of martensite formation. The width of the platelets is between 200 and 800 nm. The grain size is in the range of 100 nm to 1 µm. Polygonized cells are also observed within the equiaxed grains, indicating that recrystallization occurs during the deposition. It is generally accepted that the fine equiaxed grains are the result of self-annealing and recrystallization of the deposit during the spraying.

A higher-magnification image of the as-sprayed structure (Fig. 8) shows diffuse grain boundaries, which indicate dislocations all along the boundaries. This effect is also a product of polyganization in the structure, which is a precursor to self-annealing and recrystallization. Furthermore, subgrain bound-

Table 3 Chemical composition of as-sprayed Ti-6Al-4V alloy

	Composition, wt.%				Composition, ppm		
Element	25-45 µm	45-63 µm	63-75 µm	Element	25-45 µm	45-63 µm	63-75 µm
Al	4.6	5.28	5.7	C	160	<100	170
V	4.25	4.02	4.16	O	1380	1110	1260
Fe	0.092	0.082	0.07	H	1030	840	670
Ni	0.02	0.017	0.011	N	1290	750	850
Cr	0.014	0.016	0.015	…	…	…	…
Ti	Balance	Balance	Balance	…	…	…	…

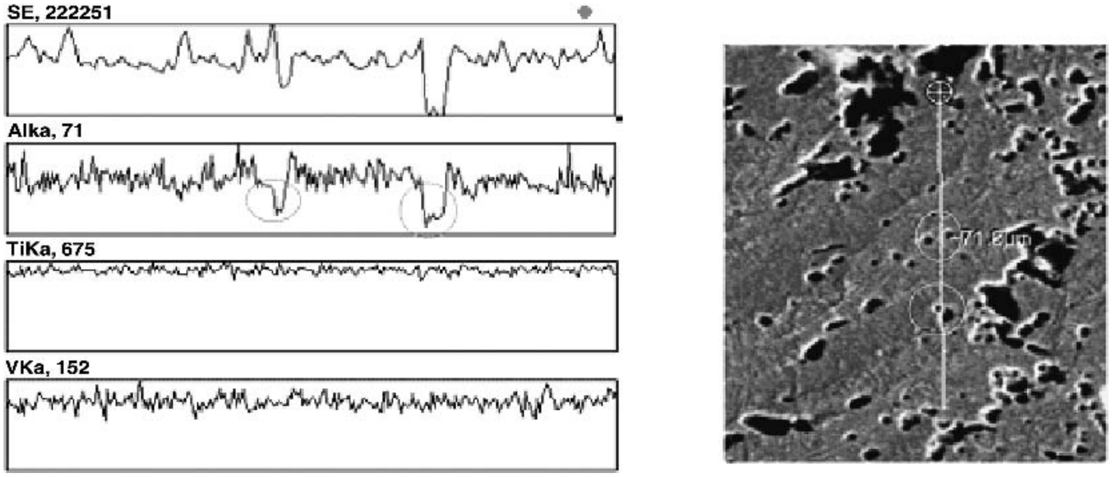

Fig. 3 Line scan from a cross section of the as-sprayed Ti-6Al-4V alloy

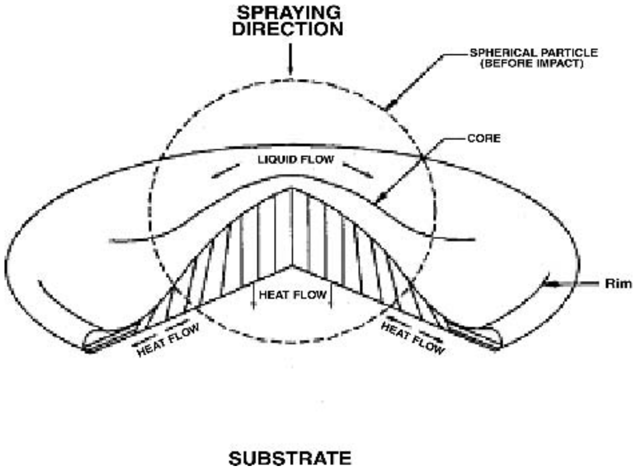

Fig. 4 Columnar structure and heat transfer in a solidifying splat (Ref 5)

aries could be observed inside the α′ platelets. These grain boundaries can form during recrystallization through the rearrangement of dislocations, forming low-angle grain boundaries and therefore reducing the residual stress of the structure. Mechanical twins or stress-induced martensite was observed in the microstructure, which is marked with arrows in Fig. 8.

3.2.4 Phase Composition. The recent models for the solidification of the individual splats would suggest a columnar grain growth within the lamellae. The columnar grains can be formed by heterogeneous nucleation of the solid phases on the mandrel or prior deposit. According to the cooling rate in VPSF, a martensitic transformation to the metastable α′-phase would be expected. The XRD pattern of the as-sprayed sample is shown in Fig. 9 compared with the calculated reference patterns of both α-hexagonal and β-bcc Ti. A closer examination of the {002} reflection of the main phase reveals a shoulder. Its position, marked with an arrow, matches well with the strongest reflection {110} of βTi (Ref 7). A detailed profile-fitting analysis

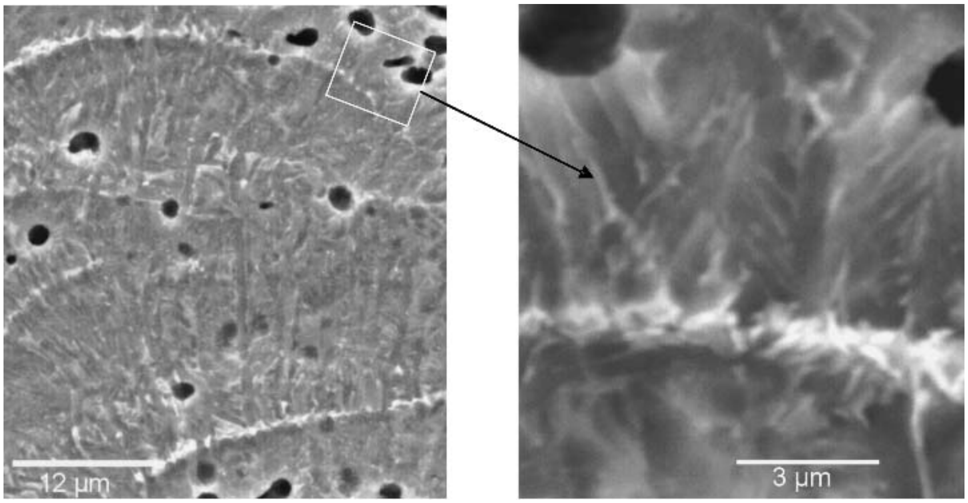

Fig. 5 SEM micrographs from a cross section of the VPSF Ti-6Al-4V alloy

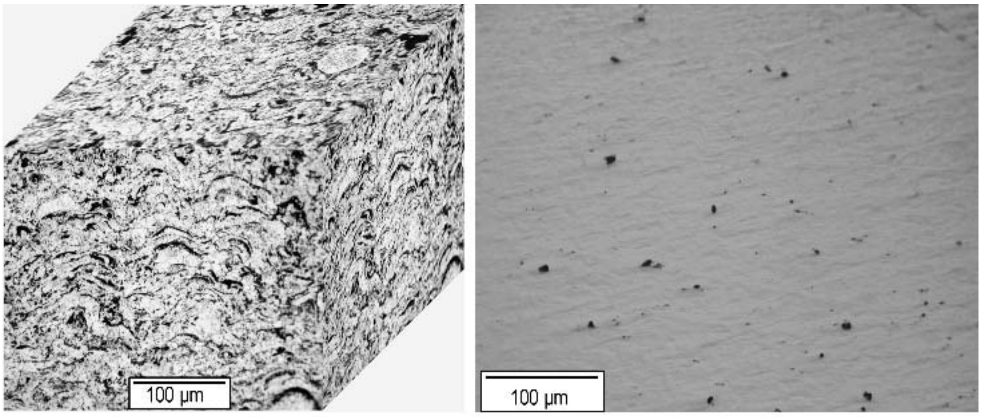

(a) (b)

Fig. 6 Optical micrograph from a cross section of the VPSF Ti-6Al-4V alloy: (a) etched; (b) unetched

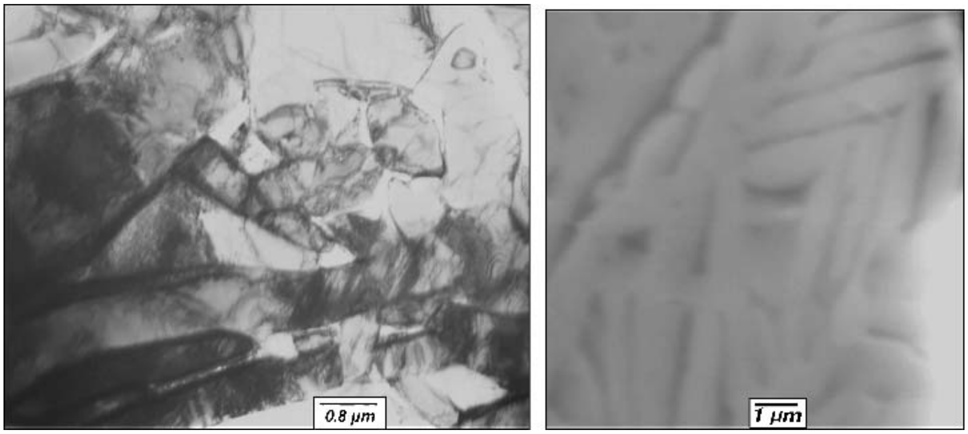

Fig. 7 TEM micrograph from lamellae and equiaxed grains in the VPSF Ti-6Al-4V alloy

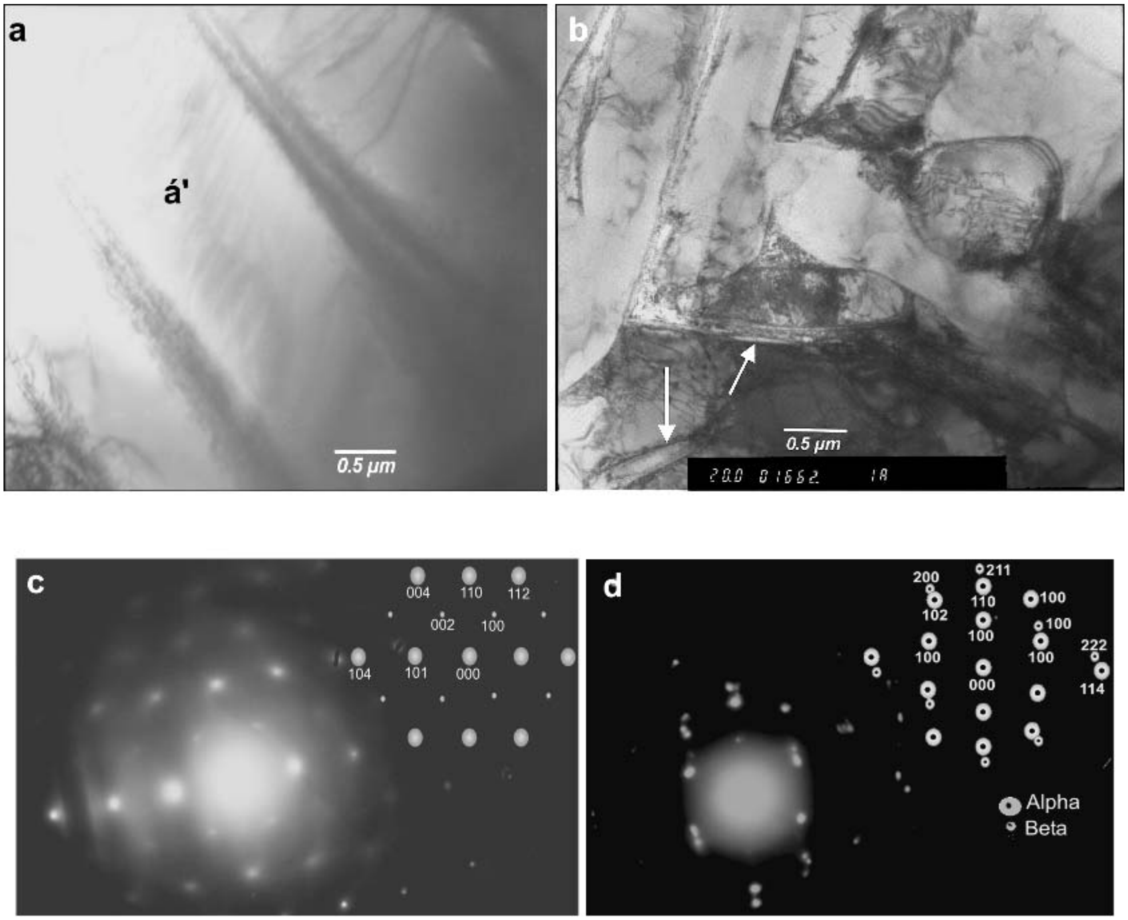

Fig. 8 Micrographs from a lateral section of the as-sprayed structure: (a) a bright field (BF) image of α' platelets and diffuse grain boundaries; (b) a BF image of mechanical twins and stress-induced martensite; (c) the selected area diffraction pattern (SADP) from α'-phase in Fig. 8(a); and (d) the SADP from platelets grain boundary

of this region of the pattern is shown in Fig. 10, and it confirms the presence of the βTi as a minor phase in the sample.

A quantitative analysis was performed on the diffraction pattern of the sample using the full-profile technique. The experimental diffraction pattern was refined in all intensity points with the two theoretical patterns until the best fit was reached. The relative amount of both components is calculated by a direct composition of the integrated areas under the all-observed peak's profiles with those of the reference patterns, taking into account the scale factors evaluated during the least-square re-

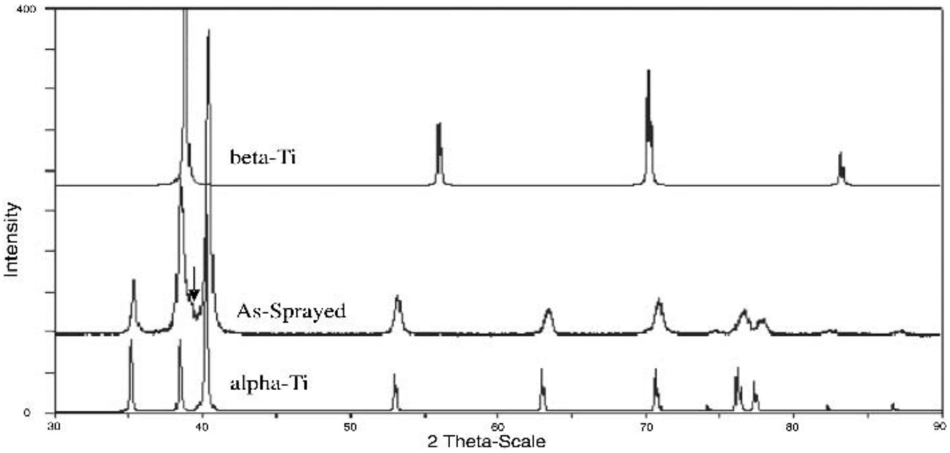

Fig. 9 XRD pattern of as-sprayed Ti-6Al-4V alloy. The position of an overlapped peak that could belong to the main 110 reflection of the bcc βTi is marked with an arrow.

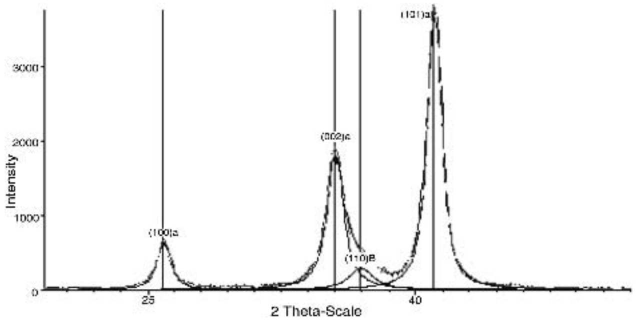

Fig. 10 Profile fittion (deconvolution) of a part of diffraction pattern of the as-sprayed sample. The small deconvoluted peak at 39° 2θ represents a minor phase with the structure of βTi.

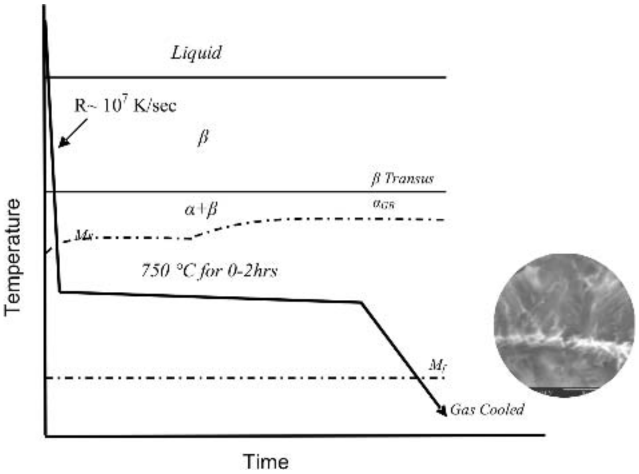

Fig. 11 Schematic representation of the cooling rate of the VPSF Ti-6Al-4V alloy

finement procedure. Unfortunately, the extensive overlapping of the peaks limits the precision of the analysis, which yields a phase composition of approximately 90 wt.% α′Ti and ≤10 wt.% βTi. The main phase, α′Ti, has lattice parameters that are smaller than that of the reference. The unit cell least-square refinement yields the lattice parameters as the following: a = 2.932(5) A°; c = 4.675(9) A°; and V = 34.8(9) A^{o3}. All reflections are quite broad. This means that the major phase in the sample, the hexagonal, αTi type, has a strained lattice. The calculated microstrain τ (Ref 8) in this sample lies within the range of 0.6 to 0.8. This is consistent with the interpretation that in the as-sprayed structure the major phase is a metastable α′Ti phase, which forms due to a martensitic transformation during cooling.

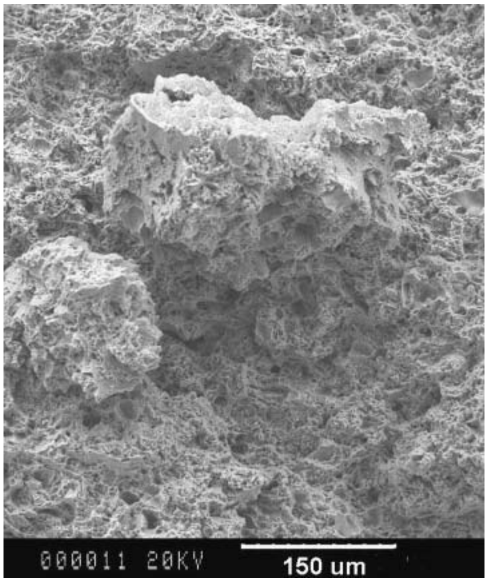

Fig. 12 Tensile-overload fracture surface of the as-sprayed Ti-6Al-4V alloy

3.2.5 Phase Formation. Based on the analyses described above, a cooling curve is presented in Fig. 11, which shows schematically the thermal history of the deposit. The droplet was cooled down and solidified from a molten state to the β-phase, and then entered the two-phase α + β field of the phase diagram at a very high cooling rate. Due to the high cooling rate, the β-transus temperature would be shifted down toward the α + β

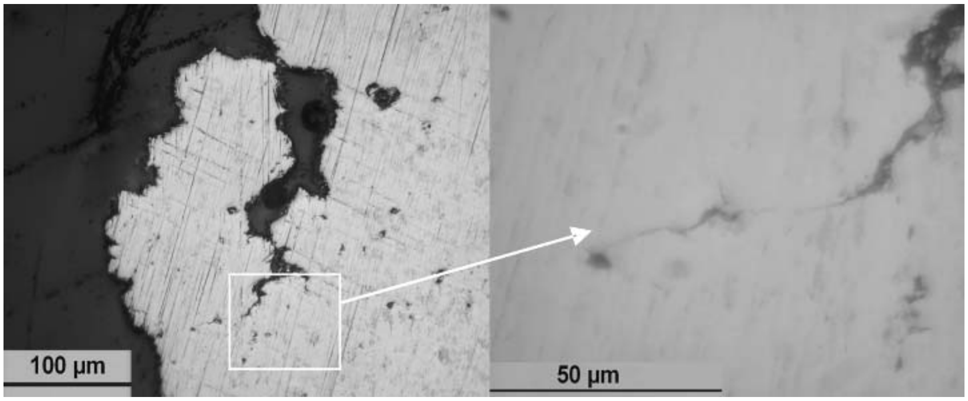

Fig. 13 A view of the area perpendicular to the fracture surface. The crack initiates and propagates through the interlamellar pores.

area compared with the equilibrium cooling condition. The critical cooling rate, r_c, the rate above which M_s becomes independent of cooling rate, decreases with increasing solute concentration. The cooling rate experienced in VPSF is clearly higher than r_c (Ref 9), thus the martensitic formation of α' is expected.

The absence of convective cooling of the deposit coupled with the very high temperature of the incoming droplets and a strong interaction between the plasma jet and deposition, kept the deposit at a relatively high temperature (~750 °C in this study) during the 1 to 2 h in which deposition was conducted. Therefore, annealing of the deposition would be expected to occur during spraying, as evidenced by the TEM observations discussed above. Oi et al. (Ref 10) have reported that the microstructure and hardness of cast specimens that are cooled slowly to room temperature after rapid cooling to 800 °C are not sensitive to cooling rates below 800 °C. The microstructure is mainly determined by the cooling rate from 1000 to 800 °C. Thus, the microstructures obtained at room temperature in this study should represent the structure established during the deposition process.

3.3 Failure Mechanism

The failure mechanism that is responsible for the low value of elongation in the as-sprayed structures (~1%) was investigated by examining the tensile fracture surfaces. The fracture surfaces at the scale of individual splats have a dimpled structure (Fig. 12). Higher-magnification views show smaller dimples that are present both at the edge of and within the large dimples. Fine-scale dimples indicate that failure occurred under nearly pure tensile conditions and that essentially no inclusions or segregation were present within the individual splats. In summary, the intrasplat fracture appears to be thoroughly ductile (Ref 11), as would be expected for the fine-scale α' structure within the splats.

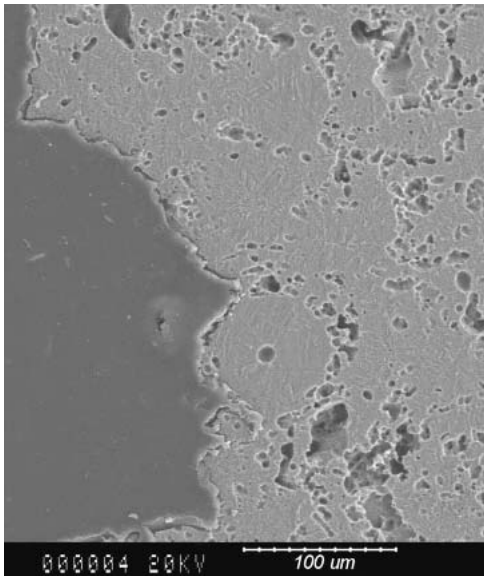

Fig. 14 A view of a polished and etched section perpendicular to the fracture surface

Figure 13 shows a polished section perpendicular to the fracture surface. A secondary crack below the fracture surface can be seen that appears to propagate from pore to pore. Figure 14 is an SEM micrograph of a polished and etched surface perpendicular to the fracture surface. There appears to be an increase in the density and size of the pores in this region adjacent to the fracture surface. Unmelted particles are frequently found on and adjacent to the fracture surface, as can be seen in Fig. 12 and 14, especially in those samples that are deposited using the fraction powder with the largest particle size. The boundaries around these unmelted particles typically have a higher density of pores than the boundaries of normal splats. These observations indicate that, although the macroscopic failure behavior could be described as brittle, the failure mechanism on a local scale does not involve brittle, cleavage fractures. Apparently, the plastic strain quickly localizes around the larger pores that are located at the splat boundaries, small pores grow, and new voids appear along the boundaries. Damage quickly accumulates along the splat boundaries, eventually linking up to form cracks (Ref 12-18).

4. Conclusion

The as-sprayed microstructure, phase formation, mechanical properties, and failure mechanism of the VPSF Ti-6Al-4V alloy were discussed in the present report. The as-sprayed structure of material deposited by VPSF consists of individual splats with a columnar grain structure within the central core. The phase composition is approximately 90% α'-phase plus residual β-phase. IA yielded a porosity level of 3% to 5%, located primarily at splat boundaries and adjacent to unmelted particles. The low elongation (~1%) was found to be due to damage accumulation at the splat boundaries, based on observations of fracture surface features.

Acknowledgments

The authors would like to thank the Natural Science and Engineering Research Council of Canada (NSERC) for their financial support. The authors also wish to acknowledge PyroGenesis Inc. for its technological support.

References

1. Y.Y. Zhao, P.S. Grant, and B. Cantor, Modeling and Experimental Analysis of Vacuum Plasma Spraying: Part I. Prediction of Initial Plasma Properties at Plasma Gun Exit, *Model. Simul. Mater. Sci. Eng.,* Vol 8, 2000, p 497-513
2. Y.Y. Zhao, P.S. Grant, and B. Cantor, Modeling and Experimental Analysis of Vacuum Plasma Spraying: Part II. Prediction of Temperatures and Velocities of Plasma Gases and Ti Particles in a Plasma Jet, *Model. Simul. Mater. Sci. Eng.,* Vol 8, 2000, p 515-540
3. T. McKechine, Near-Net Shape Spray Forming-Metals, *Thermal Spray Coatings: Research, Design, and Applications,* C. Berndt and T.F. Bernecki, Ed., ASM International, 2000, p 1105-1116
4. R.P. Krepski, *Thermal Spray Coating Applications in the Chemical Process Industries*, Vol 42, MTI Publication, Georgetown, PA, 1993
5. S. Sampath and H. Herman, Rapid Solidification and Microstructure Development During Plasma Spray deposition, *J. Thermal Spray Technol.,* Vol 5 (No. 4), 1996, p 445-456
6. H.D. Steffens and M. Dvork, Structure and Electrochemical Behavior of Vacuum Plasma Sprayed Titanium and Plasma Beam Alloyed Titanium Coatings, *Thermal Spray Research and Applications,* C. Berndt and T.F. Bernecki, Ed., ASM International, 1991, p 207-210
7. S. Malinov, W. Sha, Z. Guo, C.C. Tang, and A.E. Long, Synchrotron X-Ray Diffraction Study of the Phase Transformations in Titanium Alloys, *Mater. Charact.,* Vol 48, 2002, p 279-295
8. B.D. Cullity, *Elements of X-ray Diffraction,* 2nd ed., Addison-Wesley Publishing Co., Reading, MA, 1978
9. R. Boyer, G. Welsch, and E.W. Collings, Ed., *Materials Properties Handbook: Titanium Alloys,* 2nd ed., ASM International, 1998, p 12-48
10. K. Oi, H. Terashima, and K. Suzuki, Control of Microstructure in Ti-6Al-4V Castparts, *Metallurgy and Technology of Practical Titanium Alloys,* S. Fujishiro, D. Eylon, and T. Kishi, Ed., The Minerals Metals & Materials Society, Warrendale, PA, 1994, p 219-224
11. K. Mills, Ed., *Metals Handbook: Fractography,* 9th ed., ASM International, 1987, p 441-455
12. S. Sampath and H. Herman, Microstructure of Vacuum Plasma Sprayed Coating, *Thermal Spray Technology-New Ideas and Processes,* D.L. Houck, Ed., ASM International, 1989, p 1-7
13. J.A. Hines, J.O. Peters, and G. Lutjering, Microcrack Propagation in Ti-6Al-4V Alloys, *Fatigue Behavior of Titanium Alloys,* R. Boyer and D. Eylon, Ed., The Minerals Metals & Materials Society, Warrendale, PA, 1999, p 15-22
14. R.R. Holmes and D.H. Burns, Vacuum Plasma Spray Forming NARloy-Z and Inconel Components for Liquid Rocket Engines, *Thermal Spray Research and Applications,* T.F. Bernecki, Ed., ASM International, 1991, p 363-368
15. H.R. Salimijazi, T.W. Coyle, J. Mostaghimi, and L. Leblanc, Microstructural Formation of VPSF Ti-6Al-4V Alloys, *Thermal Spray 2003: Advancing the Science and Applying the Technology,* B.R. Marple and C. Moreau, Ed., May 5-8, 2003 (Orlando, FL), ASM International, 2003, p 611-616
16. L. Leblanc, H. R. Salimijazi, J. Mostaghimi, and T.W. Coyle, On Vacuum Plasma Spray Forming of Ti-6Al-4V, *Thermal Spray 2003: Advancing the Science and Applying the Technology,* B.R. Marple and C. Moreau, Ed., May 5-8, 2003 (Orlando, FL), ASM International, 2003, p 603-609
17. T.A. Brzezinski, S. Grenier, M.E. Smagoriski, and G.E. Kim, Vacuum Plasma Spray Deposition of Spherical Plasma Atomized Ti-6Al 4V, *Thermal Spray Coatings: Research, Design, and Applications,* C. Berndt and T.F. Bernecki, Ed., ASM International, 2000, p 935-939
18. F.H. Froes and D. Eylon, Powder Metallurgy of Ti Alloys, *Titanium Technology,* F.H. Froes, D. Eylon, and H.B. Bomberger, Ed., Titanium Development Association, Dayton, OH, 1985, p 49-58